Hindawi
International Journal of Chemical Engineering
Volume 2018, Article ID 9487486, 11 pages
https://doi.org/10.1155/2018/9487486

Research Article

Synthesis of $NiO/Y_2O_3/ZrO_2$ Catalysts Prepared by One-Step Polymerization Method and Their Use in the Syngas Production from Methane

Yvan J. O. Asencios[1] **and Elisabete M. Assaf**[2]

[1]*Instituto do Mar, Universidade Federal de São Paulo, 11030-100 Santos, SP, Brazil*
[2]*Instituto de Química de São Carlos, Universidade de São Paulo, 13560-970 São Carlos, SP, Brazil*

Correspondence should be addressed to Yvan J. O. Asencios; yvan.jesus@unifesp.br

Received 18 February 2018; Revised 30 May 2018; Accepted 10 July 2018; Published 23 August 2018

Academic Editor: Bhaskar Kulkarni

In this work, the production of Syngas (H_2/CO) from oxidative reforming of methane (ORM) and partial oxidation of methane (POM) over $NiO/Y_2O_3/ZrO_2$ catalysts was studied. The nickel concentration was varied (ranging from 0 to 40 wt.%) aiming to optimize the performance in ORM and POM reactions; these reactions were carried out at 750°C and 1 atm for 6 hours. The catalysts were prepared by the one-step polymerization method (OSP) and characterized by different techniques. This method led to production of materials of smaller crystallite size than others of similar composition prepared under other methods; the catalysts presented good nickel dispersion, well-defined crystalline structure, and well-defined geometrical morphology. Additionally, the OSP method was advantageous because it was carried out in a single calcination step. The catalyst containing 20% wt. of nickel (20Ni20YZ sample) showed the highest methane conversion, high selectivity to H_2 and CO, low carbon deposition rates, and, curiously, the best geometric morphology. The results of this paper also demonstrated that the nickel concentration in the mixture strongly influenced the morphology of the catalysts; therefore, the morphology also influenced the catalytic performances during the Syngas production reactions.

1. Introduction

Methane is found mainly in biogas, natural gas, and shale gas. Biogas is a renewable alternative source of methane and is considered a first-generation biofuel. The production of the biogas occurs in the absence of oxygen where anaerobic bacteria break down the organic matter, producing methane and carbon dioxide as major products, and other gaseous by-products such as H_2S, NH_3, and H_2, in smaller amounts [1, 2].

Syngas (synthesis gas, a mixture of H_2/CO) is a raw material of high value which is used as the starting material in the production of synthetic fuels such as di-methyl ether (DME), methanol, and liquid hydrocarbons (by the Fischer–Tropsch process). Biogas can be transformed into Syngas through reforming reactions as reported in the literature [2–7]. Thus, the biogas can be transformed by dry reforming of methane (DRM, reaction (1)) and partial oxidation of methane (POM, reaction (2)), resulting in the oxidative reform of methane (ORM, reaction (3)):

$$\text{DRM: } CH_4 + CO_2 \longrightarrow 2CO + 2H_2 \qquad \Delta H^0_{298K} = 260.5 \text{ kJ} \cdot \text{mol}^{-1} \tag{1}$$

$$\text{POM: } CH_4 + 0.5O_2 \longrightarrow CO + 2H_2 \qquad \Delta H^0_{298K} = -22.6 \text{ kJ} \cdot \text{mol}^{-1} \tag{2}$$

$$\text{ORM: } 1.5CH_4 + CO_2 + 0.25O_2 \longrightarrow 2.5CO + 3H_2 \qquad \Delta H^0_{298K} = 249.2 \text{ kJ} \cdot \text{mol}^{-1} \tag{3}$$

Carbon dioxide and methane are the two principal components of biogas, and the main greenhouse gases, so its transformation into Syngas may have very beneficial results

from an environmental point of view. It is known that catalysts based on noble metals corresponding to the Group VIIIB are good catalysts for reforming methane (e.g., Pt, Rh, Pd, and Ru), demonstrating high selectivity for hydrogen, high methane conversion, and low carbon deposition rates (carbon is an undesired product). The catalysts based on nonnoble metals of Group VIIIB (Ni, Co, and Fe) have shown catalytic activity in methane reforming reactions, similarly to that of noble metals based catalysts, and they are low cost; however, nonnoble metals result in high carbon deposition rates [6, 8, 9].

The actual Syngas production by industry (for hydrogen generation) is based on the steam reforming of methane (SRM, reaction (4)), which uses a nickel catalyst supported on alumina; however, nickel catalysts present problems due to carbon deposits which deactivate the catalyst (covering the active metallic sites) and moreover, its accumulation increases the reactor pressure, leading to explosion hazards. Many efforts have been directed to decrease carbon deposits [10, 11].

$$\text{SRM: } CH_4 + H_2O \longrightarrow CO + 3H_2 \qquad \Delta H^0_{298K} = 225.4 \text{ kJ} \cdot \text{mol}^{-1} \tag{4}$$

Several ways have been proposed for the formation of carbon deposits in methane reforming reactions; among them, the methane molecule cracking (reaction (5)) and the Boudouard reaction (reaction (6)) can lead to catalyst deactivation:

$$CH_4 \longrightarrow C + 2H_2 \quad \Delta H^0_{298K} = 75 \text{ kJ} \cdot \text{mol}^{-1} \tag{5}$$

$$2CO \longrightarrow C + CO_2 \quad \Delta H^0_{298K} = -173 \text{ kJ} \cdot \text{mol}^{-1} \tag{6}$$

The water-gas shift reaction (WGSR) is a reversible exothermic reaction, and the opposite direction is favored at high temperatures. So the reverse reaction (RWGSR, reaction (7)) is very likely to occur during methane reforming and POM reaction:

$$CO_2 + H_2 \longleftrightarrow CO + H_2O \quad \Delta H^0_{298K} = 41 \text{ kJ} \cdot \text{mol}^{-1} \tag{7}$$

The following solutions have been proposed to minimize the carbon deposits: (a) new catalyst preparation method aiming to decrease the crystallite size of the catalytic phase [7, 12, 13], (b) the use of catalytic supports based on solid solutions with the formation of oxygen vacancies [5, 6, 9, 14], (c) the use of hydrotalcites as catalyst precursor [15], and (d) the addition of noble-metal promoters to the catalysts [16, 17], among others.

Regarding to preparation methods of catalysts, Mori et al. [18] prepared NiO/YSZ catalysts (where YSZ means Y_2O_3-ZrO_2 solid solution) by impregnation method; the NiO content of these catalysts was 60% wt. They reported that the average crystallite size of NiO in their NiO/YSZ catalyst was <60 nm (calculated from XRD analysis). In the same report, the NiO size for the same mixture, but prepared by the solid-state reaction method, was 7 μm. Resini et al. [19] also prepared the NiO/YSZ catalyst by impregnation method (the nickel content was 50% wt.), and reported the formation of heterogeneous morphology, as the former NiO particles showed large sizes (crystallites larger than 40 nm, according to TEM analysis), and YSZ reached approximately 5 nm.

Similarly, Bellido et al. [20] prepared the NiO/YSZ catalysts, and Y_2O_3-ZrO_2 support was prepared by polymerization method (Y/Z molar ratio of 12%), and the nickel was incorporated by the impregnation method, and the nickel content was 5% wt. According to them, the average crystallite size of NiO of these catalysts (calculated from the Scherrer equation) was 25.9 nm.

In our previous reports [21, 22], we reported that the one-step polymerization method improved the catalytic activity of Co_3O_4/CeO_2, and NiO/MgO-ZrO_2 catalysts in the steam reforming of bioethanol and in the oxidative reform of methane, respectively. The average crystallite sizes of NiO were smaller than those reported in [18–20], where the precipitation method was employed.

The polymerization method forms a homogeneous material with a fine dispersion of the components of the catalysts (owing to the atomistic distribution of the metal cations during polymerization) [20–22]. In view of the referenced reports, the objective of the present paper was to study the $NiO/Y_2O_3/ZrO_2$ mixture containing various nickel contents (ranging from 0 to 40 wt.%) in the Y_2O_3/ZrO_2 support (Y/Z ratio of constant composition) synthesized by the one-step polymerization method (OSP method). The $NiO/Y_2O_3/ZrO_2$ catalysts were characterized and tested in the oxidative reform of methane (ORM) and in the partial oxidation of methane (POM). In this paper, we report the optimal nickel concentration (wt.%) for a good catalytic performance in the ORM and POM reactions, and additionally, we found that (under OSP method) the nickel concentration led to catalysts with different morphologies (clear and well defined forms). Among other factors, such as crystalline structure, nickel charge, metallic dispersion, and surface area; the morphology of each catalyst influenced the catalytic performance in the reactions studied.

2. Methodology

2.1. Preparation of Catalysts. The catalyst preparation method in this study was the one-step polymerization method. In this method, the ability of the organic hydroxycarboxylic acids (citric acid in this case) to chelate with most cations was used. Ethylene-glycol (a polyhydric alcohol), when added to the chelate with adequate heating, leads to the formation of a polyester due to successive condensation reactions between the alcohol and the acid chelate. The polymerization method has been used by several researchers due to the high homogeneity of the material produced, compared to precipitation, coprecipitation, and impregnation methods [20, 21, 23]. In this sense, the present study used the one-step polymerization method, where the support precursor and the catalytic phase were mixed together (in a single step).

The catalysts were prepared by the one-step polymerization method using $Ni(NO_3)_2{\cdot}6H_2O$, $Zr(CO_3)_2{\cdot}1{\cdot}5H_2O$, $Y(NO_3)_3{\cdot}6H_2O$, citric acid, and ethylene-glycol, in accordance with the method described in the literature [5, 20, 22]. The salts of the catalyst precursor were previously dissolved

(carbonate in nitric acid and nitrates in water). In this method, the precursor salts were dissolved, respectively, and mixed together forming a single solution. This solution was added to the mixture composed of ethylene-glycol and citric acid in the proportion of 1 mol of Zr per 3 mol of citric acid and a mass ratio of 60 : 40 between the citric acid and ethylene-glycol. The resulting solution produced a translucent resin. The polymerization process occurred at 120°C for 12 hours. After obtaining the polymers, they were subjected to calcination in two consecutive stages: first, under air flow at 500°C (5°C·min $^{-1}$) for 3 h and second, under the same air flow but at 750°C (5°C·min^{-1}) for 2 h. The resulting materials were powdered in a porcelain mortar and pestle.

The Y_2O_3 content was kept constant at 20 mol% relative to ZrO_2. The nickel content was varied as follows: 0%, 10%, 20%, and 40% relative to the total weight of the catalyst. The catalysts were named 20YZ, 10Ni20YZ, 20Ni20YZ, and 40Ni20YZ according to the percentage of Ni in the total catalyst weight. The catalyst 20YZ corresponds to the pure catalytic support (without nickel, Ni 0%).

2.2. Characterization of the Catalysts. The crystalline phases were identified by X-ray diffraction analysis (XRD) in a Rigaku Multiflex diffractometer (30 kV, 10 mA), in the $2\theta = 5$–80° range and speed $2^\circ\,\text{min}^{-1}$ using Cu-K α radiation ($\lambda = 1.5406$ Å), and the diffraction patterns were identified by comparison with the database of the International Centre for Diffraction Data (JCPDS). The average crystallite sizes were determined from XRD line-broadening measurements using the Scherrer equation [24]: $d = k{\cdot}\lambda/(\beta_{\text{hkl}}{\cdot}\cos\theta)$, where d is the average crystallite size, k is the shape factor, taken as 0.89, λ is the wavelength of CuKα radiation, β_{hkl} is the full width at half maximum (FWHM) of the particular peak, and θ is Bragg's angle.

In the temperature programmed reduction analyzes (TPR), 100 mg of catalysts were used, a gas mixture of 1.96% H_2/Ar with a flow of 30 mL·min^{-1} and a heating rate of 5°C min^{-1} up to a temperature of 1000°C. The surface area measurements were performed on a Quantachrome Nova 1200 equipment, and the results of nitrogen adsorption were treated according to the BET method.

The analysis by SEM-EDX was particularly suitable for the study of the morphology of solids. For this analysis, a small amount of the fresh catalyst was placed in isopropyl alcohol to form a suspension. The suspension was dropped slowly onto an aluminum plate to obtain maximum dispersion of the powder in the sample holder. The apparatus used consists of LEO-440 electron microscope with Oxford detector operating at 20 kV electron beam. For each analysis, the samples were sputter-coated with gold.

The *in situ* XRD analyzes were carried out using a diffractometer (Huber) in the Brazilian Synchrotron Light Laboratory (LNLS) in Campinas, Brazil, in the D10B-XPD light-line. The wavelength used for each analysis was 1.5406 Å. Each analysis explored the region of $2\theta = 25$–70°. The catalyst was placed in a sample holder in a temperature programmable oven. In this system, the catalysts were placed in contact with the respective flow gas: N_2 under ambient conditions and H_2 reduction condition, so that the first XRD pattern was obtained under ambient temperature in a N_2 stream (100 mL·min^{-1}) and the second was collected on the reduced catalyst with H_2 (5% H_2/He, 50 mL·min^{-1}) at a temperature of 800°C.

2.3. Catalytic Tests. The catalytic tests were carried out in a fixed-bed down-flow reactor (internal diameter = 10 mm) with 100 mg of catalyst. Before each reaction, the catalysts were reduced at 800°C for 1 h, under flowing H_2 (30 mL·min^{-1}). The sample was then brought to the reaction temperature (750°C for all reactions conditions) under pure N_2 flow.

The catalysts were tested under two conditions:

(a) Oxidative reforming of methane (ORM): the feed was a mixture of gases (60% CH_4 and 40% CO_2) and synthetic air (O_2: 21%, N_2: 79%) reaching a molar ratio of $1.5CH_4 : 1CO_2 : 0.25O_2$, giving a total flow of 107 mL·min^{-1}, inside the reactor. The conversion of CH_4 and CO_2 was calculated, respectively, as

$$R_{\text{conversion}}\,(\%) = \frac{R_{\text{in}} - R_{\text{out}}}{R_{\text{in}}} \times 100, \tag{8}$$

where R is the molar flow rate (mol·min^{-1}) of CH_4 or CO_2.

The selectivity was calculated as

$$\text{selectivity}_{R_i} = \frac{R_{i\ \text{produced}}}{R_{\text{CH}_4\ \text{converted}} + R_{\text{CO}_2\ \text{converted}}} \times 100, \tag{9}$$

where "R_i" is the molar flow rate (mol·min^{-1}) of the product (H_2 or CO).

(b) Partial oxidation of methane (POM): the feed was a mixture of gases in molar proportion of $2CH_4 : 1O_2$, stoichiometric for the POM, giving a total flow of 107.3 mL·h^{-1}. Oxygen was added as synthetic air (79% N_2, 21% O_2). The CH_4 conversion was calculated as

$$R_{\text{conversion}}\,(\%) = \frac{R_{\text{in}} - R_{\text{out}}}{R_{\text{in}}} \times 100, \tag{10}$$

where R is the molar flow rate (mol·min^{-1}) of CH_4.

The selectivity was calculated as

$$\text{selectivity}_{R_i} = \frac{R_{i\ \text{produced}}}{R_{\text{CH}_4\ \text{converted}}} \times 100, \tag{11}$$

where "R_i" is the molar flow rate (mol·min^{-1}) of the product (H_2 or CO or CO_2).

Carbon deposition was determined as the apparent gain in mass of the catalyst after each reaction (mmol·C·h^{-1}).

The gaseous reactants and products were analyzed on a gas chromatograph (Varian, Model 3800), in line with the catalytic unit test. The chromatograph includes two thermal conductivity detectors and 13X molecular sieve packed columns (this column uses N_2 as carrier for analysis of H_2

gas) and Porapak N (this column uses He as the carrier for the analysis of CO_2 gas, CH_4, and CO). The reaction temperature was controlled and measured by a thermocouple inserted into the top of the catalyst bed.

3. Results and Discussion

3.1. Characterization of the Catalysts. The XRD patterns of the catalysts were recorded *in situ* under ambient conditions and under reduction conditions in the presence of H_2 at 800°C, these results are shown in Figures 1 and 2, respectively. Supplementary Figure 1S shows the XRD patterns of the fresh support (20YZ) and pure ZrO_2 (prepared under the same conditions as the 20YZ support); in this figure, one can observe that pure ZrO_2 presents peaks attributed to the tetragonal (T) and monoclinic (M) phase of zirconia; the Y_2O_3/ZrO_2 mixture in the 20YZ support led to the stabilization of the zirconia tetragonal phase. The tetragonal phase of zirconia is stabilized due to the formation of the Y_2O_3-ZrO_2 solid solution in the mixture; in this solid solution, Y^{3+} ions dissolved in the ZrO_2 network lead to the formation of oxygen vacancies for charge compensation effects, between Y^{3+} and Zr^{4+} (to maintain net neutrality in the network) [5, 9, 20].

Figure 1 presents the XRD patterns for the fresh catalysts under ambient conditions, and the average crystallite sizes (using the Scherrer equation [24]) are shown in Table 1. As expected, the higher nickel content in the catalysts favored the formation of larger NiO crystallites. Contrarily, the average crystallite sizes of zirconia decreased for catalysts with higher nickel content, suggesting that high nickel content (which formed larger NiO crystallites) hinders the ZrO_2 crystal growth. The YZ mixture is constant in the composition of each catalyst. In the OSP method studied in the present paper, the precursors of Ni, Y, and Zr were dissolved before the polymerization process. During the thermal treatment of the polymers performed to obtain the solid oxides with the corresponding crystalline phase, solid reactions, combustion reactions, and crystal growth took place. Therefore, we suggest that the presence of high Ni content in the catalysts hinders the crystal growth of ZrO_2 during the thermal treatment. This is similar to the finding by Denrya et al. [25] and Trusova et al. [26] who studied in detail the effect of thermal treatment on the crystal growth of solid oxides.

This might also explain the continuous decrease of the oxide catalyst surface area (Table 1) when the nickel content was increased.

The surface area values of each material are shown in Table 1. The surface area decreased in the following order: 10Ni20YZ ($30\ m^2 \cdot g^{-1}$) > 20Ni20YZ ($17\ m^2 \cdot g^{-1}$) > 40Ni20YZ ($13\ m^2 \cdot g^{-1}$). In this context, the NiO crystallites of large size may cover the surface pores of the support 20YZ ($39\ m^2 \cdot g^{-1}$) leading to a continued decrease of surface area in each catalyst.

In Figure 2, the reduction of NiO to Ni° can be observed; the catalysts with higher nickel content led to the formation of larger Ni° crystallites (Table 1). It is also observed that the Ni° particles tend to sinter under reduction conditions

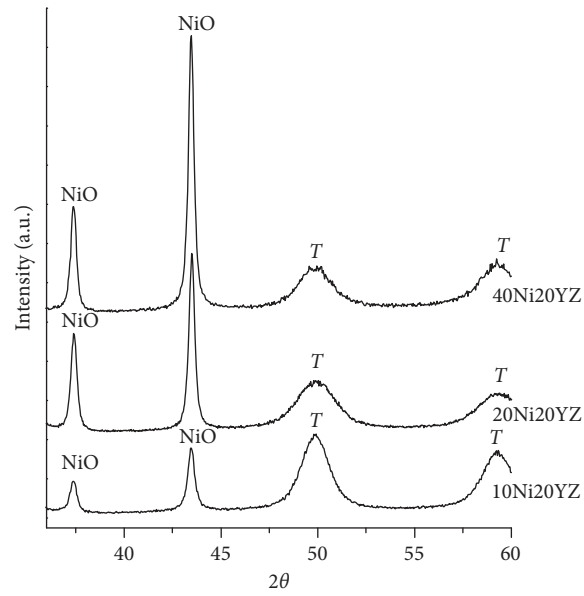

Figure 1: In situ XRD patterns of catalysts at room temperature (in the $2\theta = 35$–$60°$ range, speed $2°\,min^{-1}$ using Cu Kα radiation ($\lambda = 1.5406$ Å), the diffraction patterns were identified by comparison with the database of the International Centre for Diffraction Data—JCPDS).

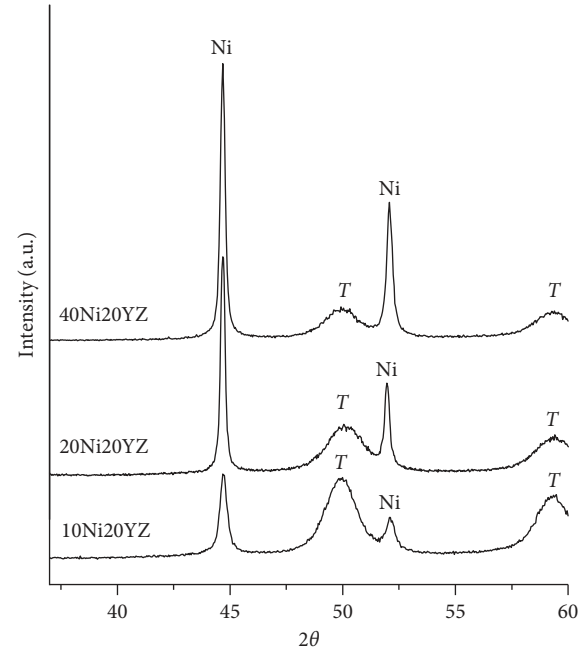

Figure 2: In situ XRD patterns of reduced catalysts. The XRD pattern was collected on the reduced catalyst with H_2 (5% H_2/He, $50\ mL \cdot min^{-1}$) at a temperature of 800°C; the diffraction patterns were identified by comparison with the database of the International Centre for Diffraction Data—JCPDS.

(800°C) and form larger crystallites than their corresponding oxides (NiO) for each catalyst. The increase in crystallite size in the 10Ni20YZ catalyst shows that at this nickel concentration, the sintering is poor (when compared with the other samples with higher nickel concentration).

Table 1: Physical-chemical properties of the catalysts and TPR analyses results.

Sample	Average crystallite size (nm)			% reduction of NiO (TPR)	Surface area ($m^2 \cdot g^{-1}$)	Metallic dispersion (D_M)
	ZrO_2	NiO	Ni°			
20YZ	7.2	—	—	—	39	—
10Ni20YZ	5.1	14.8	15.0	50	30	6.7
20Ni20YZ	4.9	19.0	25.8	67	17	3.9
40Ni20YZ	4.3	27.6	33.1	81	13	3.0

The smallest crystallite size of Ni° and NiO was obtained in sample 10Ni20YZ (15 nm).

Mori et al. [18] reported that the average crystallite size of NiO in their NiO/YSZ catalyst (where YSZ means Y_2O_3-ZrO_2 solid solution) was <60 nm (calculated from XRD analysis); this catalyst was obtained by the impregnation method. This NiO size for the same mixture, but prepared by the solid-state reaction method, was 7 μm. The NiO content of these catalysts was 60% wt.

Resini et al. [19] also studied the NiO/YSZ catalyst and reported the formation of heterogeneous morphology, as the former NiO particles showed large sizes (crystallites larger than 40 nm, according to TEM analysis), and YSZ reached approximately 5 nm. This catalyst was prepared by the impregnation method, and the nickel content was 50% wt.

Bellido et al. [20] reported the average crystallite size (calculated from the Scherrer equation) of NiO of 25.9 nm, for NiO/YSZ catalyst, Y_2O_3-ZrO_2 support was prepared by the polymerization method (Y/Z molar ratio of 12%), and the nickel was incorporated by the impregnation method, the nickel content was 5% wt.

Considering the average crystallite size of NiO reported in our study (Table 1) and compared with that obtained by Mori et al. [18], Resini et al. [19], and Bellido et al. [20]; we suggest that the OSP method produced smaller crystallite size than that reached by the referred authors. Additionally, the OSP method was very practical, since the three Ni, Zr, and Y oxides were obtained in a single step, where only one calcination procedure was needed.

Similarly, Youn et al. [27] obtained a NiO/YSZ catalyst, where the catalytic support was obtained by the templating sol-gel method, and nickel was incorporated by the incipient wetness impregnation method. The nickel concentration used was 20% wt. The Ni/ZrO_2 catalyst formed Ni° with an average crystallite size of 22 nm (calculated by the Scherrer equation); however after adding Y_2O_3 to reach the Y/Z molar ratio of 0.2 (similar molar ratio as employed in our paper for YZ support), the Ni° crystallite size reached 15 nm and the Y_2O_3-ZrO_2 support reached 6.4 nm.

Although Youn et al. [27] obtained smaller crystallite sizes than those obtained by our OSP method, the crystallite size values shown in Table 1 are relatively close to those of the referred study; and moreover, we prepared the catalysts using a single calcination step, where support and catalytic phase were obtained together (the referenced authors used a two-step calcination).

The estimated metal dispersion (D_M) calculated from the Ni° crystallites size [24, 28–30] is found in Table 1. According to these values, as expected, the 10Ni20YZ sample has the highest dispersion Ni°, probably owing to the low nickel concentration in the catalyst composition and due to the OSP method employed. The lowest metallic dispersion was found for the sample with the highest nickel content (40Ni20YZ).

According to the TPR profiles of the catalysts shown in Figure 3, a single reduction peak is observed below 550°C which was attributed to reduction of NiO in different interactions with the support.

In the 10Ni20YZ profile sample, the major part of the single NiO peak (located at interval 350°C–550°C) corresponds to NiO species weakly interacting with the YZ support. Furthermore, it is noted that increasing the nickel content produced the extension of this single peak to higher temperatures, suggesting the increase of NiO species that go to the bulk part and the increase of the interaction with the YZ support. This is reasonable, since Ni^{2+} and Y^{3+} can form the NiO-Y_2O_3 solid solution at 750°C in the presence of air, as was described in our previous report [5]. The two peaks located above 550°C correspond to the reduction of surface oxygen atoms located in the close vicinity of the oxygen vacancies of the support 20YZ [18, 22, 27].

Figures 4–6 show SEM images of the fresh catalysts; it was also possible to map the Ni and Zr elements for each SEM image by energy-dispersive X-ray spectroscopy (EDX-mapping for Ni and Zr are shown in Supplementary Figures S2–S4). Figure 4 shows that the 10Ni20YZ catalyst morphology presents irregularly shaped particles (agglomerate species) that are repeated on the surface. According to the mapping on this region of the sample (Supplementary Figure S2), the major composition of these agglomerates is Zr (the Y mapping image was very similar to Zr). Additionally, according to the Ni mapping of 10Ni20YZ catalysts (Supplementary Figure S2), the small agglomerates with diameter size ranging from 1 to 3 μm (some indicated with green circles in Figure 4) are mainly composed of Ni. These analyses suggest that the low nickel content (10%) led to a good dispersion of NiO particles on the surface of the solid solution Y_2O_3-ZrO_2 (YZ support).

Figure 5 shows the image of the 20Ni20YZ catalyst obtained by SEM analysis. The morphology of this catalyst shows the formation of a solid in the cubical form. According to the mapping in this region (Supplementary Figure S3), the cube-form solid is primarily formed by Zr (the Y mapping image was very similar to Zr), and the small spheres around 3 μm in diameter (well-formed) on the surface of the cube are composed principally of Ni.

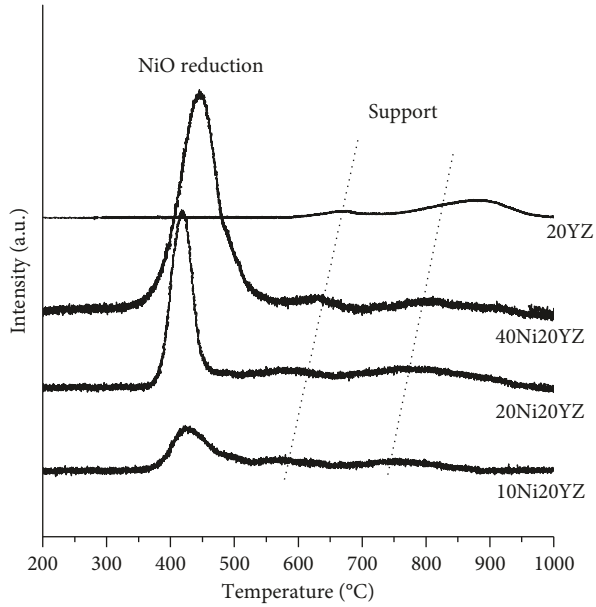

Figure 3: Results for temperature programmed reduction with H_2 (H_2-TPR) of the catalysts. In the H_2-TPR analyzes 100 mg of catalysts, a gas mixture of 1.96% H_2/Ar (flow at 30 mL·min^{-1}) and a heating rate of 5°C min^{-1} (from room temperature to 1000°C) were used.

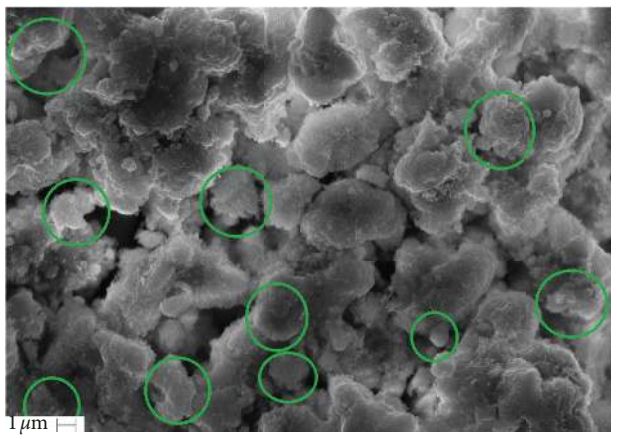

Figure 4: SEM image (×10000) of 10Ni20YZ catalyst before reaction.

This analysis indicates that the 20% Ni content is a suitable concentration for the NiO/Y_2O_3/ZrO_2 mixture, as it resulted in an optimal arrangement of the catalytic phase on the support, where the NiO particles are in good dispersion on the surface of the Y_2O_3-ZrO_2 solid solution formed by 20YZ.

Figure 6 shows the SEM image of the 40Ni20YZ catalyst. In this figure, the formation of two cube-shaped solids (named YZ in the figure) with agglomerated particles in their close vicinity, in almost the entire region of the image shown, can be clearly observed. According to the mapping in this region (Supplementary Figure S4), the two cube-shaped solids (YZ) are principally composed of Zr (the image of Y mapping was very similar to that of Zr), and the agglomerate particles in their vicinity are principally composed of Ni

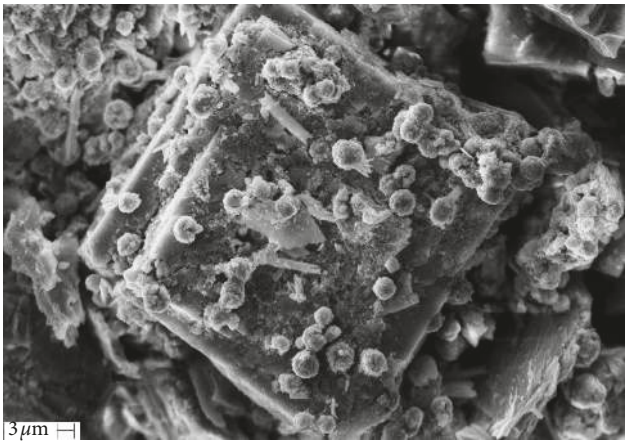

Figure 5: SEM image (×3000) of 20Ni20YZ catalyst before reaction.

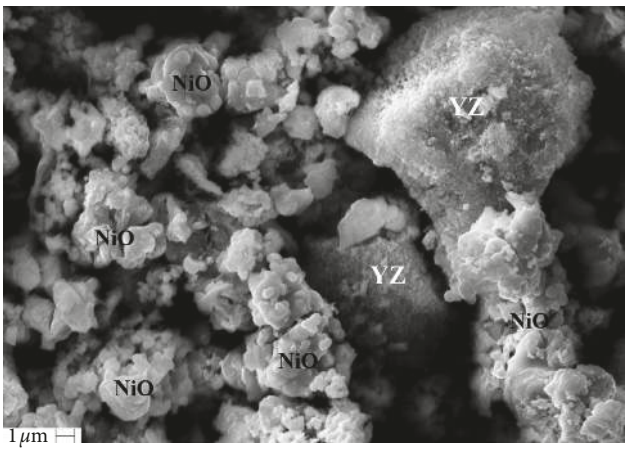

Figure 6: SEM image (×3000) of 40Ni20YZ catalyst before reaction.

(named as NiO in the Figure 6). These results suggest that the large amount of nickel in the 40Ni20YZ catalyst composition led to the formation of many agglomerated NiO particles, thus resulting in poor dispersion of the active phase on the catalyst support.

The NiO particle dispersion located in different regions of each catalyst, presented in the SEM images, followed the same trend as that found for the estimated metallic dispersion (Table 1; after reduction of the catalysts with H_2); in this context, 10Ni20YZ and 40Ni20YZ presented the highest and the lowest nickel dispersion (resp.) among all catalysts.

3.2. Catalytic Tests

3.2.1. Oxidative Reform of Methane (ORM). The CH_4 and CO_2 conversion values and the H_2/CO ratio in the oxidative reform of methane over each catalyst are shown in Figure 7 and Supplementary Figure S5, respectively. The results show that the optimal nickel content was 20% wt. since the highest reactant conversions were found for the 20Ni20YZ catalyst.

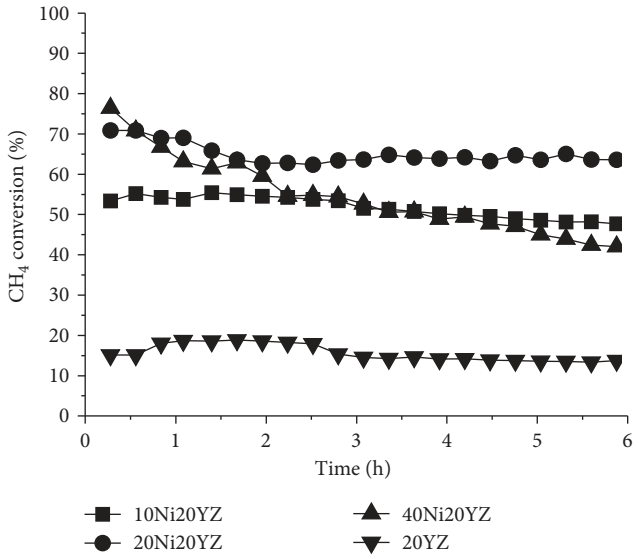

Figure 7: Conversion of CH_4 results obtained during the catalytic tests in the oxidative reform of methane at 750°C (molar ratio of reactants $1.5CH_4 : CO_2 : 0.25O_2$; molar total flow: 107 mL·min^{-1}).

The content of 40% wt. of nickel present in the 40Ni20YZ catalyst was too high for the catalyst, leading to catalyst low stability and deactivation during the reaction. The catalyst with 10% wt. of nickel content (10Ni20YZ) showed good stability, but low conversion values. The carbon deposition rates were 0.10 (10Ni20YZ); 0.14 (20Ni20YZ); and 0.39 (40Ni20YZ) mmolC·h^{-1}. These results suggest that there was a good distribution of the Ni° active centers on the Y_2O_3-ZrO_2 solid solution in the 20Ni20YZ, thus leading to a high conversion of CH_4, CO_2, and O_2 into H_2 and CO and to a low carbon deposition rate value (0.14 mmolC·h^{-1}). Since it is known that the Y_2O_3-ZrO_2 solid solution produce oxygen vacancies, which can help the removal of carbon deposits during the reforming reaction [5, 6, 9, 20], we suggest that oxygen vacancies of this solid solution may have favored the carbon removal in 20Ni20YZ, in a greater extent.

The conversion profile of the 40Ni20YZ catalyst (Figure 7) shows a continuous fall along the reaction. This decrease is due to the high nickel concentration in this catalyst which led to deactivation. This is expected, since the high nickel content in the 40Ni20YZ catalyst caused sintering of the Ni° particles after the reduction process, as seen in the *in situ* XRD analysis under reducing conditions with H_2 (see Table 1; the 40Ni20YZ catalyst had the largest crystallite size of Ni°, 33 nm). It is known that large Ni° crystal structures lead to high carbon deposition rates, producing incrustation of carbon on the active metal and causing deactivation of the catalyst-active sites. This may explain the high carbon deposition rates and poor catalytic performance recorded by the 40Ni20YZ catalyst (0.39 mmol·h^{-1}). Furthermore, according to the TPR analyses (Figure 3), this sample has a large proportion of NiO species interacting weakly with the catalytic support that reduced at low temperatures. These species could be facilitating their sintering. This was evidenced by the SEM analysis where the 40Ni20YZ catalyst morphology image showed the formation of many agglomerated NiO particles situated around the cube-shaped solids of Y_2O_3-ZrO_2 solid solution (see Figure 6 and Supplementary Figure S4).

As noted in the estimation of the metallic phase dispersion, the 10Ni20YZ catalyst showed the highest metallic dispersion (6.7%) among all samples. This was also suggested by SEM analyzes of this catalyst, where the morphology showed the formation of small NiO agglomerates spaced apart (Figure 4 and Supplementary Figure S2). However, the 10% Ni content seems to be too low for higher conversion values; this high dispersion favored a good stability during the catalytic reaction.

We suggest that the Y_2O_3-ZrO_2 support and the Ni°-active sites are in good proportion in the 20Ni20YZ catalyst, thus leading to high conversion values and a relatively low carbon deposition rate. By analyzing the 20Ni20YZ images obtained by SEM analysis (Figure 5 and Supplementary Figure S3), it can be claimed that there was good conformation of the NiO particles on the catalyst support. Furthermore, in this sample, the NiO particles are present as small spheres deposited on the surface of the Y_2O_3-ZrO_2 catalytic support (which shows the symmetrical shape-cubes). This good conformation of the catalytic phase/catalytic support also explains the good catalytic performance of the 20Ni20YZ sample.

After the catalytic tests, traces of water, as a by-product, were collected and they showed the occurrence of the RWGSR reaction ($CO_2 + H_2 \longleftrightarrow CO + H_2O$). The occurrence of this reaction can explain the fact that the CO_2 conversion is slightly higher than the CH_4 conversions (Supplementary Figure S5 and Figure 7).

The CO_2 percentages involved in RWGSR (values calculated from the collected water) were 16%, 14%, and 19% for samples 10Ni20YZ, 20Ni20YZ, and 40Ni20YZ, respectively. These values indicate that the 20Ni20YZ sample showed the lowest water formation value and the best reactant conversion values.

Supplementary Figure S6 shows the H_2/CO molar ratio in the reaction products during oxidative reform of methane over the catalysts. These values are always lower than 1.2, which is the stoichiometric ratio for this reaction (reaction (3)). The low values of the H_2/CO molar ratio on 10Ni20YZ and 40Ni20YZ samples are consistent with the low conversion values and high contributions to RWGSR (16% and 19% of the CO_2 in the feed stream, resp.); this reaction uses hydrogen and carbon dioxide molecules to produce water.

3.2.2. Partial Oxidation of Methane (POM). Figure 8 and Supplementary Figures S7 and S8 show the results of the POM reaction over the catalysts. Figure 8 shows the CH_4 conversion profiles against reaction time; in this figure, it can be seen that the conversion of methane decreased as follows: 40Ni20YZ > 20Ni20YZ > 10Ni20YZ > 20YZ, in other words, with decreasing nickel content. Catalytic activity of sample 40Ni20YZ decreased gradually during the reaction time, demonstrating instability owing to deactivation, probably because of the high nickel content which favors sintering, as seen in characterization results. The carbon deposition rates

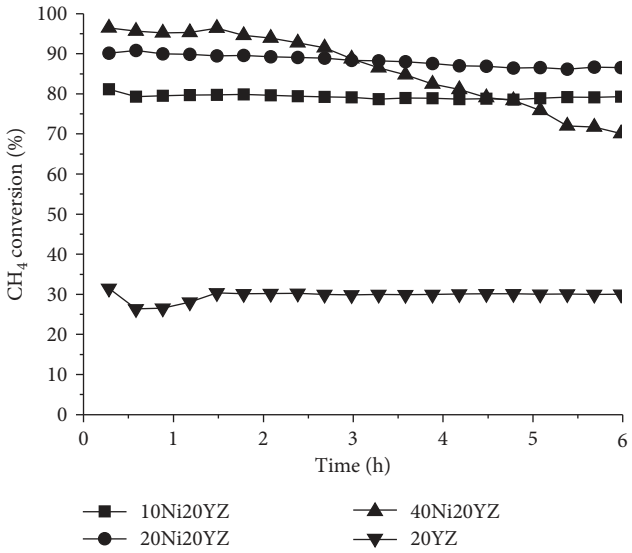

Figure 8: Conversion of CH_4 results obtained during the partial oxidation of methane over the catalysts at 750°C (molar ratio of reactants in the inlet stream: $2CH_4:1O_2$; molar total flow 107 mL·min^{-1}).

rose monotonically with nickel content on the catalysts 10Ni20YZ, 20Ni20YZ, and 40Ni20YZ; they were 0.08, 0.10, and 0.32 mmol·h^{-1}, respectively. These values indicate that 20Ni20YZ showed the best performance in the POM reaction, because it achieved a conversion high rate (Figure 8), relatively low carbon deposition, as well as the highest selectivity for hydrogen (Supplementary Figure S7).

The highest H_2/CO ratios were produced by samples 20Ni20YZ and 10Ni20YZ and were around 1.7, which is nearly stoichiometric. The low H_2/CO values for 40Ni20YZ are in agreement with the deactivation on this catalyst. The H_2/CO values above the stoichiometric value (approximately 2) can be due to other reactions occurring in parallel with POM, as will be discussed in the following paragraphs.

The presence of H_2O (traces collected at the end of reaction time) and CO_2 during each catalytic test indicates that the POM occurred through the combustion-reforming mechanism on the catalysts. This mechanism is described by the following reactions [31, 32]:

$$\text{TCM: } CH_4 + 2O_2 \longrightarrow CO_2 + 2H_2O \qquad \Delta H^0_{298K} = -890 \text{ kJ} \cdot \text{mol}^{-1} \tag{12}$$

The global sum of reactions (12) + (1) + 2 × (4) is reaction (2), with a H_2/CO ratio of 2. Additionally, under the presence of CO_2 and H_2 in the reaction products, the reverse water-gas shift reaction (RWGSR) (7) is very likely to occur; this reaction is favored at high temperature:

The occurrence of the RWGSR and the combustion-reforming mechanism explains why the H_2/CO ratios for all samples were above the stoichiometric value. The selectivity results for H_2 and CO_2 are shown in Supplementary Figures S7 and S8, respectively. The selectivity for H_2 and CO followed a trend similar to that of CH_4 conversion, the selectivity for H_2 and CO decreased as follows: 40Ni20YZ > 20Ni20YZ > 10Ni20YZ > 20YZ, and the selectivity for H_2 and CO over sample 40Ni20YZ decreased continuously during the reaction, probably owing to sintering which led to the high amount of coke recorded for this sample.

Samples 10Ni20YZ and 20Ni20YZ reported low CO_2 selectivity; contrarily, 20YZ and 40Ni20YZ samples were the most selective for CO_2. The trend found in CO_2 selectivity indicates that the catalytic support (20YZ) strongly favors the TCM (reaction (7)); the gradual loss of Ni°-active sites of the 40Ni20YZ catalyst during the POM reaction favored the TCM reaction (expressed by the gradual increase of selectivity to CO_2). Probably, the oxygen vacancy formation in the 20YZ support, which activates O_2 molecules (O_2 + active site → $O_{(s)} + O_{(s)}$), is favoring the TCM reaction and therefore the production of CO_2 over the 20YZ support.

From the results of the ORM and POM catalytic tests, we suggest that the catalysts 10Ni20YZ, 20Ni20YZ, and 40Ni20YZ have two types of active sites: the first is the Ni° site that dissociates the CH_4 molecules and the second is the Y_2O_3-ZrO_2 solid solution (which is known to form oxygen vacancies) that may promote the O_2 and CO_2 molecules [33, 34].

The SEM image of some catalyst (in a region rich in carbon, according to EDX analysis) after OPM reaction is shown in Figures 9 and 10. Figure 9 corresponds to 20Ni20YZ (our best catalyst) after POM; according to this image, very few carbon filaments were formed, the morphology of the carbon is mostly amorphous on the surface of the catalyst (the SEM image of sample 20Ni20YZ after ORM is shown in Supplementary Figure S9, and this image is very similar to the same catalyst after POM). Figure 10 corresponds to 40Ni20YZ after POM; in this case, the carbon was entirely amorphous. The results of the characterization of the spent catalysts suggest that the catalyst synthesized by the OSP method forms graphitic carbon of amorphous morphology. The variation of the nickel charge in the catalyst formulation did not markedly influence the carbon deposit morphology.

The XRD patterns of spent catalysts after 6 h of POM (see Figure S11, in the Supplementary) showed the formation of graphitic carbon, which is clearly observed (peak at 26°) over 20Ni20YZ and 40Ni20YZ catalysts. The peak related to graphitic carbon was not observed on the XRD pattern of spent 10Ni20YZ catalyst. Not significant difference was observed for coke by XRD analysis of spent catalysts after ROM.

A long-term stability test was carried out on the best catalyst in the present study (20Ni20YZ), which was tested under POM reaction conditions for 24 hours. The results are included in the Supplementary Figure S10), where it can be seen that the catalyst maintained its activity for 24 h. A slight continuous decrease in the reactant conversion rates was observed during the reaction, but this seemed to stabilize after 6 hours of reaction, as after this time, the conversion value remained constant at 85%. The coke deposition rate over 24 h was 0.12 mmol·h^{-1} on 20Ni20YZ, this value being close to that found for the catalytic test over 6 h of reaction. The stability test of 20Ni20YZ catalyst in ORM was reported previously for us in [5].

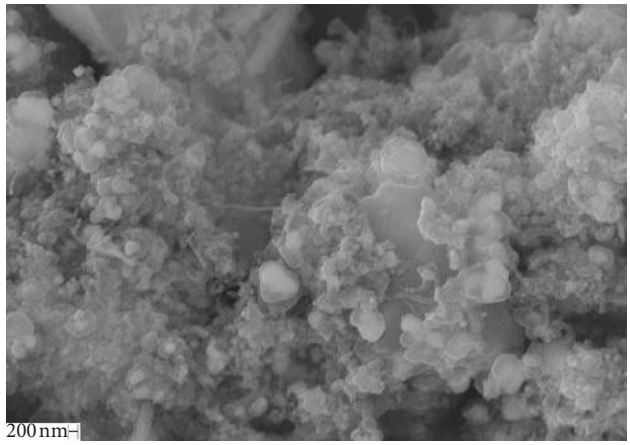

Figure 9: SEM image of sample 20Ni20YZ (×50000) after POM reaction.

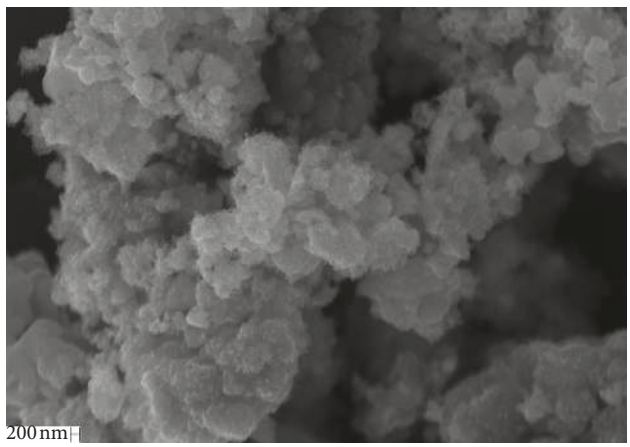

Figure 10: SEM image of sample 40Ni20YZ (×25000) after POM reaction.

4. Conclusions

The production of Syngas from methane through the POM and ORM over the catalysts rose as the Ni content increased, and the optimal nickel content in the $NiO/Y_2O_3/ZrO_2$ mixture prepared under the OSP method was 20% wt. (for both reactions). At this nickel concentration, high selectivity to H_2 and CO, and low carbon deposition rates were reported; curiously the fresh catalyst at this concentration showed the best geometric morphology. Further nickel content led to catalyst deactivation.

The variation of the charge of NiO in the $NiO/Y_2O_3/ZrO_2$ mixture under the OSP method led to NiO of face-centered cubic phase and to the tetragonal zirconia (demonstrated by its stabilization forming Y_2O_3-ZrO_2 solid solution in the support). According to SEM/EDX analysis, different nickel charges formed catalysts with different morphologies, NiO particles were located at different places on the surface of the Y_2O_3-ZrO_2 support, and the catalysts 20Ni20YZ and 40Ni20YZ showed well defined geometrical morphology.

From the results of the catalytic tests, we suggest that the catalysts have two types of active sites: the first is the Ni° site that dissociates the CH_4 molecules and the second is the Y_2O_3-ZrO_2 solid-solution (present in the support) that may promote the O_2 and CO_2 molecules.

The characterization of the catalysts demonstrated that the nickel concentration in the mixture influenced the catalyst morphology; therefore, the morphology also influenced the catalytic performances during the Syngas production reactions. The variation of the nickel charge in the formulation of the catalyst influenced the carbon deposition rates, but did not markedly influence the morphology of the carbon deposit.

The OSP method led to production of materials of smaller crystallite size as others of similar composition, but prepared under other methods; additionally, this was advantageous because it was carried out in a single calcination step.

Data Availability

The data used to support the findings of this study are available from the corresponding author upon request.

Conflicts of Interest

The authors declare that there are no conflicts of interest regarding the publication of this paper.

Acknowledgments

The authors thank the São Paulo Research Foundation (FAPESP) for the financial support (Grant no. 2014/24940–5), the Brazilian National Council for Scientific Development (CNPq) for the scholarship and the grant, and the Brazilian Synchrotron Light Laboratory (LNLS) for the *in-situ* XRD conducted in the D10B-XPD line.

Supplementary Materials

The supplementary material contains Figure S1 which shows the XRD patterns of the fresh 20YZ support and pure ZrO_2 in the $2\theta = 20–40^{\circ}$ range (speed $2^{\circ}\,min^{-1}$ using Cu-K α radiation, $\lambda = 1.5406$ Å) to complement the XRD discussion of the manuscript. EDX mapping at the regions of SEM image of Figure 4 (10Ni20YZ), Figure 5 (20Ni20YZ), and Figure 6 (40Ni20YZ) are shown in Figure S2, Figure S3, and Figure S4, respectively. The conversion of CO_2 and H_2/CO molar ratio obtained during the catalytic tests in the oxidative reform of methane at 750°C over the catalysts is shown in Figure S5 and Figure S6, respectively. The selectivity to hydrogen and to carbon dioxide (mol produced/mol of CH_4 converted) obtained during the partial oxidation of methane over the catalysts at 750°C is shown in Figure S7 and Figure S8, respectively. SEM image of sample 20Ni20YZ after ORM reaction (×25 000) is shown Figure S9. Figure S10 shows the stability test of 20Ni20YZ catalysts for OPM reaction. Figure S11 shows the XRD patterns for spent catalysts after POM reaction. Finally, Figure S12 shows the graphical abstract of this manuscript. (*Supplementary Materials*)

References

[1] S. N. Naik, V. V. Goud, P. K. Rout, and A. K. Dalai, "Production of first and second generation biofuels: a comprehensive review," *Renewable and Sustainable Energy Reviews*, vol. 14, no. 2, pp. 578–597, 2010.

[2] L. Pengmei, Z. Yuan, C. Wu, L. Ma, Y. Chen, and N. Tsubaki, "Bio-syngas production from biomass catalytic gasification," *Energy Conversion and Management*, vol. 48, no. 4, pp. 1132–1139, 2007.

[3] N. Rueangjitt, C. Akarawitoo, and S. Chavadej, "Production of hydrogen-rich syngas from biogas reforming with partial oxidation using a multi-stage AC gliding arc system," *Plasma Chemistry and Plasma Processing*, vol. 32, no. 3, pp. 583–596, 2012.

[4] M. Benito, S. García, P. Ferreira-Aparicio, L. García-Serrano, and L. Daza, "Development of biogas reforming Ni-La-Al catalysts for fuel cells," *Journal of Power Sources*, vol. 169, no. 1, pp. 177–183, 2007.

[5] Y. J. O. Asencios, C. B. Rodella, and E. M. Assaf, "Oxidative reforming of model biogas over NiO-Y_2O_3-ZrO_2 catalysts," *Applied Catalysis B: Environmental*, vol. 132-133, pp. 1–12, 2013.

[6] Y. J. O Asencios, P. A. Nascente, and E. M. Assaf, "Partial oxidation of methane on NiO-MgO-ZrO_2 catalysts," *Fuel*, vol. 97, pp. 630–637, 2012.

[7] A. F. Lucrêdio, J. M. Assaf, and E. M. Assaf, "Methane conversion reactions on Ni catalysts promoted with Rh: influence of support," *Applied Catalysis A: General*, vol. 400, no. 1-2, pp. 156–165, 2011.

[8] P. Kumar, Y. Sun, and R. O. Idem, "Nickel-Based ceria, zirconia, and ceria–zirconia catalytic systems for low-temperature carbon dioxide reforming of methane," *Energy and Fuels*, vol. 21, no. 6, pp. 3113–3123, 2007.

[9] J. D. A. Bellido and E. M. Assaf, "Effect of the Y_2O_3-ZrO_2 nickel catalyst support composition on evaluated in dry reforming of methane," *Applied Catalysis A: General*, vol. 352, no. 1-2, pp. 179–187, 2009.

[10] J. R. Rostrup-Nielsen and J. H. Back-Hansen, "CO_2 Reforming methane over transition metals," *Journal of Catalysis*, vol. 144, no. 1, pp. 38–49, 1993.

[11] V. A. Tsipouriari, A. M. Efstathiou, Z. L. Zhang, and X. E. Verykios, "Reforming of methane with carbon dioxide to synthesis gas over supported Rh catalysts," *Catalysis Today*, vol. 21, no. 2-3, pp. 579–587, 1994.

[12] Y. J. O. Asencios and E. M. Assaf, "Combination of dry reforming and partial oxidation of methane on NiO-MgO-ZrO_2 catalyst: effect of nickel content," *Fuel Processing Technology*, vol. 106, pp. 247–252, 2013.

[13] S. O. Soliviev, K. A. Yu, S. N. Orlyk, and E. V. Gubareni, "Carbon dioxide reforming of methane on monolithic Ni/Al_2O_3-based catalysts," *Journal of Natural Gas Chemistry*, vol. 20, no. 2, pp. 184–190, 2011.

[14] F. L. S. Carvalho, Y. J. O Asencios, A. M. B. Rego, and E. M. Assaf, "Hydrogen production by steam reforming of ethanol on Co_3O_4/La_2O_3/CeO_2 catalysts," *Applied Catalysis A: General*, vol. 483, pp. 52–62, 2014.

[15] A. R. Gonzalez, Y. J. O Asencios, E. M Assaf, and J. M Assaf, "Dry reforming of methane on Ni–Mg–Al nano-spheroid oxide catalysts prepared by the sol–gel method from hydrotalcite-like precursors," *Applied Surface Science*, vol. 280, pp. 876–887, 2013.

[16] A. F. Lucrêdio, J. M. Assaf, and E. M. Assaf, "Reforming of a model biogas on Ni and Rh Ni catalysts: effect of adding La," *Fuel Processing Technology*, vol. 102, pp. 124–131, 2012.

[17] A. F. Lucredio, G. T. Filho, and E. M. Assaf, "Co/Mg/Al hydrotalcite-type precursor, promoted with La and Ce, Studied by XPS and applied to methane steam reforming reactions," *Applied Surface Science*, vol. 255, no. 11, pp. 5851–5856, 2009.

[18] H. Mori, C. J. Wen, J. Otomo, K. Eguchi, and H. Takahashi, "Investigation of the interaction between NiO and yttria-stabilized zirconia (YSZ) in the NiO/YSZ composite by temperature-programmed reduction technique," *Applied Catalysis A: General*, vol. 245, no. 1, pp. 79–85, 2003.

[19] C. Resini, M. C. Herrera-Delgado, S. Presto et al., "Yttria-stabilized zirconia (YSZ) supported Ni–Co alloys (precursor of SOFC anodes) as catalysts for the steam reforming of etanol," *International Journal of Hydrogen Energy*, vol. 33, no. 14, pp. 3728–3735, 2008.

[20] J. D. A. Bellido, E. Y. Tanabe, and E. M. Assaf, "Carbon dioxide reforming of ethanol over Ni/Y_2O_3–ZrO_2 catalysts," *Applied Catalysis B: Environmental*, vol. 90, no. 3-4, pp. 485–488, 2009.

[21] F. L. S. Carvalho, Y. J. O. Asencios, J. D. A. Bellido, and E. M. Assaf, "Bio-ethanol steam reforming for hydrogen production over Co_3O_4/CeO_2 catalysts synthesized by one-step polymerization method," *Fuel Processing Technology*, vol. 142, pp. 182–191, 2016.

[22] Y. J. O. Asencios, J. D. A. Bellido, and E. M. Assaf, "Synthesis of NiO-MgO-ZrO_2 catalysts and their performance in reforming of model biogas," *Applied Catalysis A: General*, vol. 397, no. 1-2, pp. 138–144, 2011.

[23] P. J. Marcos and D. Gouvêa, "Effect of MgO segregation and solubilization on the morphology of ZrO_2 powders during synthesis by the Pechini method," *Cerâmica*, vol. 50, no. 313, pp. 38–42, 2004.

[24] S. Chien and W. Chiang, "Catalytic properties of NiX zeolites in the presence of cerium additives," *Applied Catalysis*, vol. 61, no. 1, pp. 45–61, 1990.

[25] I. Denry, J. A. Holloway, and P. K. Gupta, "Effect of crystallization heat treatment on the microstructure of niobium-doped fluorapatite glass-ceramics," *Journal of Biomedical Materials Research Part B: Applied Biomaterials*, vol. 100, no. 5, pp. 1198–1205, 2012.

[26] E. A. Trusova, A. Khrushcheva, and L. I. Shvorneva, "The impact of thermal treatment conditions on the formation of crystalline structure of Ce-Zr-oxide composite obtained by a modified sol-gel technique," *Journal of Physics: Conference Series*, vol. 345, article 012035, 2012.

[27] M. H. Youn, J. G. Seo, J. C. Jung, S. Park, and I. K. Song, "Hydrogen production by auto-thermal reforming of ethanol over nickel catalyst supported on mesoporous yttria-stabilized zirconia," *International Journal of Hydrogen Energy*, vol. 34, no. 13, pp. 5390–539, 2009.

[28] C. H. Bartholomew and R. B. Pannell, "The stoichiometry of hydrogen and carbon monoxide chemisorption on alumina and silica-supported nickel," *Journal of Catalysis*, vol. 65, no. 2, pp. 390–401, 1980.

[29] R. D. Jones and C. H. Barthoholomew, "Improved technique for measurement of flow hydrogen chemisorption on metal catalysts," *Applied Catalysis*, vol. 39, pp. 77–88, 1988.

[30] J. Zhang, H. Wang, and A. Dalai, "Effects of metal content on activity and stability of Ni-Co bimetallic catalysts for CO_2 reforming of CH_4," *Applied Catalysis A: General*, vol. 339, pp. 121–129, 2008.

[31] Y. Q. Song, D. H. He, and B. Q. Xu, "Effects of preparation methods of ZrO_2 support on catalytic performances of Ni/ZrO_2 catalysts in methane partial oxidation to syngas," *Applied Catalysis A: General*, vol. 337, no. 1, pp. 19–28, 2008.

[32] H. Morioka, Y. Shimizu, M. Sukenobu et al., "Partial oxidation of methane to synthesis gas over supported Ni catalysts prepared from Ni-Ca/Al-layered double hydroxide," *Applied Catalysis A: General*, vol. 215, no. 1-2, pp. 11–17, 2001.

[33] W. Dow and T. Huang, "Yttria-stabilized zirconia supported copper oxide catalyst-I. Effect of oxygen vacancy of support on copper oxide reduction," *Journal of Catalysis*, vol. 160, no. 2, pp. 155–170, 1996.

[34] L. Xiancai, L. Shuigen, Y. Yifeng, W. Min, and H. Fei, "Studies on coke formation and coke species of nickel-based catalysts in CO_2 reforming of CH_4," *Catalysis Letters*, vol. 118, no. 1-2, pp. 59–63, 2007.